Performance assessment of bifacial c-Si PV modules through device simulations and outdoor measurements

Th. Katsaounis [*1,3,4], K. Kotsovos [†2], I. Gereige[2], A. Basaheeh[2], M. Abdullah[2], A. Khayat[2], E. Al-Habshi[2], A. Al-Saggaf [2], and A.E. Tzavaras[1]

[1]Computer Electrical and Mathematical Science & Engineering (CEMSE), KAUST, Thuwal, Saudi Arabia
[2]Renewable Energy, Carbon Management Division, Saudi Aramco, Thuwal, Saudi Arabia
[3]IACM, FORTH, Heraklion, Greece
[4]Dept. of Math. & Applied Mathematics, Univ. of Crete, Heraklion, Greece

Abstract

Bifacial solar cells are receiving increased attention in the PV market due to their higher energy yield compared to conventional monofacial modules thanks to additional light conversion through their back surface. This additional rear side energy gain creates a potential for significant reduction of the overall levelized cost of energy (LCOE). Despite this fact, wide deployment of bifacial PV modules is very limited because of the high unpredictability of their power output due to various factors such as ground reflectance, module elevation angle, orientation and tilt angle. Due to this complexity, modelling of bifacial modules and systems is currently not developed at the same level of maturity as monofacial ones, where established commercial tools have been developed for PV system designers. In this regard, a customized 2D device model has been developed to simulate bifacial PV structures based on the numerical solution of the transport equations by the finite element method. The model was used to simulate actual PV performance and energy yield based on measured outdoor environmental parameters including solar radiation spectrum and temperature. Bifacial device output was also compared with a monofacial one based on the industrial standard Al-BSF structure. Simulated results were also compared and validated with outdoor experimental data based on IV measurements of monofacial and bifacial modules installed at various tilt angles at a location near the Western coast of Saudi Arabia.

Keywords : customized 2D solar cell simulator, bifacial PV device, local climate conditions, hazy days favour bifacial devices

1 Introduction

Bifacial PV modules are continuously increasing their worldwide PV market share since they provide increased energy conversion compared to conventional monofacial devices due to their capability to absorb additional light through the back surface [1], [2], [3]. This fact provides a strong potential for bifacial solar modules to reduce the levelized cost of energy (LCOE) of PV generated electricity [4]. Therefore, large scale bifacial PV installations can potentially reach impressively low LCOE as already demonstrated by the worlds lowest bid for the Sakaka solar power project in Saudi Arabia [5]. Although bifacial PV structures were investigated since the 1960s [6], [7], their manufacturing process was too complicated for mass production at that time. Recent advances in industrial processes, however, have been implemented to reduce the cost of bifacial PV modules and various companies have introduced such products in their manufacturing lines [8], [9], [10], [11], therefore their market share is predicted to increase in the near

---

*theodoros.katsaounis@kaust.edu.sa(Corresponding author)
†konstantinos.kotsovos@aramco.com

future [12]. In addition, PV industry is shifting to high efficiency solar cell structures, like the passivated emitter and rear cell with local passivated contacts (PERC) [13], the n-Pasha (passivated on all sides H pattern), designed by ECN [14] and commercialized by Yingli [15], and the heterojunction PV structure originally developed by Panasonic [16], an already common technology choice for many PV manufacturers [17]. All these structures can be easily manufactured in bifacial configuration, while offering improved conversion efficiencies compared to the industrial standard Al-BSF (aluminium back surface field).

Bifacial PV modules are not widely deployed in PV system installations, however, because the evaluation of their field performance is challenging due to the variable illumination conditions on the back surface, which depend on different parameters, such as the percentage of diffuse radiation in the solar spectrum, ground reflectance, module elevation, orientation and tilt angle [1], [18]. The combinations of all these parameters complicates bifacial PV energy yield calculations and system design, thus negatively affecting the bankability of this technology. This is not the case for the standard monofacial PV's, where their performance and energy yield simulation can be easily implemented in commercially available PV software [19], [20], [21], [22]. In addition, currently available PV system design software typically use 1D circuit models for solar cell device simulations, which can be quite detailed, however they do not solve the solar cell transport equations, due to the increased computational load that is required.

In this regard, the development of a simulation software, which solves the carrier transport equations that could take into account various effects such as: the different illumination conditions on both surfaces, actual solar spectrum variations, operating temperature, various solar cell device structures and material parameters to accurately evaluate the PV module electrical output, is beneficial. This fully customized model will enable PV developers to calculate with high accuracy the optimal system design based on various available solar cell technologies, local weather parameters and PV system configuration.

Based on the above, the purpose of this study is the application of a customized model based on the solution of the solar cell device transport equations in 2D, specifically designed for bifacial solar cells similar to PERC to simulate outdoor field performance and energy yield of such devices and comparing their output gain with monofacial structures. The simulations are performed using locally measured outdoor environmental parameters including solar radiation spectrum and temperature, while calculated data are compared and validated with actual measurements on commercial monofacial and bifacial PV modules. The measurements are performed for various PV module tilt angles. The formulation of the model is based on the one developed in [23], which is extended to take into account temperature dependence of device parameters. The model with its accompanying assumptions and fitted experimental parameters is analyzed in section 2, while the experimental outdoor measurement setup is described in section 3. Simulation results and comparison with experimental data obtained from the outdoor measuring setup are presented in section 4 and an extended discussion on these results is provided in section 5. Finally, section 6 discusses the main conclusions and future perspectives of this work.

2   The mathematical model

In the previous study [23], the authors introduced a new mathematical model for PERC p-type c-Si solar cell, see Figure 1(left), based on the assumptions that there are no transient phenomena and that the cell operates in the low injection regime. In this regime the classical drift-diffusion model can be simplified considerably since diffusion dominates current transport. After an appropriate change of variables the new dimensionless system reads as follows

$$\begin{aligned}
-\Delta\eta + \eta &= g_n(z), &\quad (x,z) \in [0,L] \times [0,w], \\
-\Delta u + \eta &= g_n(z), &\quad (x,z) \in [0,L] \times [0,w],
\end{aligned} \tag{1}$$

where $u = \frac{V}{V_C}$ is a scaled voltage drop and $\eta = \frac{n}{N_A}$ is a scaled electron concentration, while L is the pitch(length) of the cell and w its width. The source $g_n(z) = \frac{L_n^2}{N_A D_n} G(z)$ describes a scaled generation rate $G(z)$ with L_n being the diffusion length, N_A is the hole doping density and D_n, D_p are the electron and hole diffusivity constants with μ_n, μ_p being the corresponding mobilities. The model is augmented with the following set of linear and nonlinear boundary conditions, [24] :

- Vertical sides: $x = 0, L, \ z \in (0, w)$,

$$\nabla\eta \cdot \zeta = 0, \quad \nabla u \cdot \zeta = 0. \tag{2}$$

2
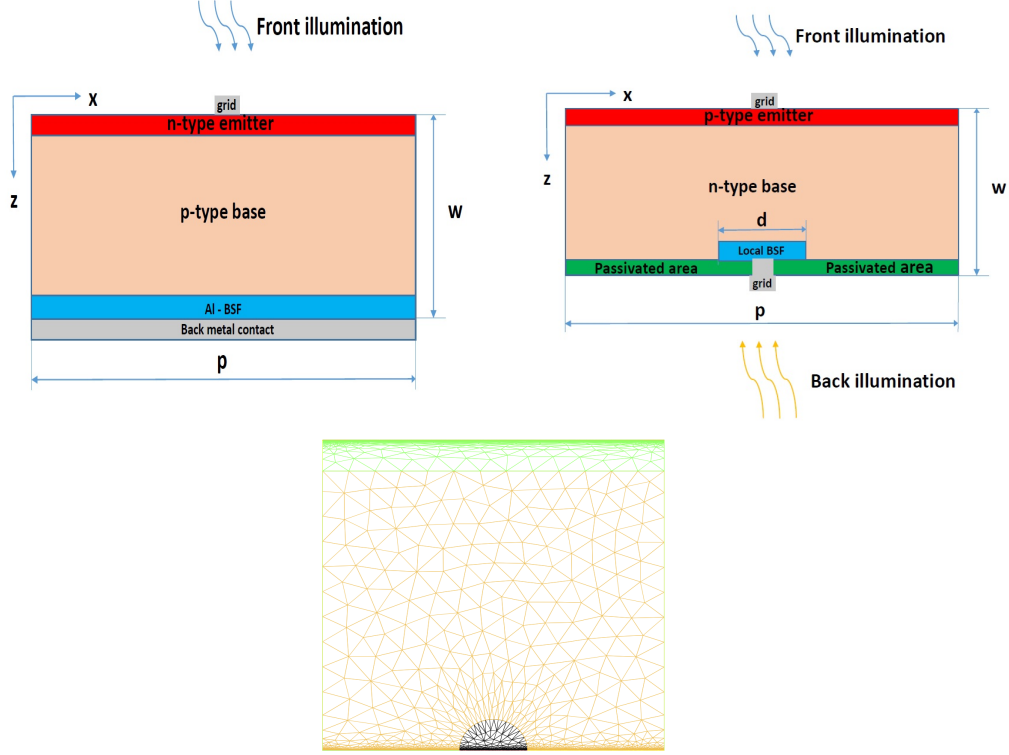
Figure 1: Geometry of a monofacial(top-left), bifacial solar device (top-right) and a representative triangulation (bottom)

- Top side: $z = 0$, $x \in (0, L)$,

$$\nu_A^2 \, \eta = \exp\left(\frac{V_C}{V_T}(V_b + u)\right) - 1, \quad \nabla u \cdot \zeta = \nu_A^2 \, j_0 \left(1 - \exp\left(-\frac{V_C}{V_T}(V_b + u)\right)\right). \tag{3}$$

- Bottom side : $z = w$, $x \in (0, L)$,

$$\nabla \eta \cdot \zeta = -s_n \, \eta,$$
$$\text{outside contact} : \nabla u \cdot \zeta = -s_n \, \eta, \tag{4}$$
$$\text{inside contact} : u = 0,$$

where ζ is the outward normal to the side, V_T is the thermal voltage and $V_C = \frac{D_n - D_p}{\mu_p}$. The recombination velocity S is : $S = s_1$ outside the contact and $S = s_2$ inside the contact. Further, n_i denotes the intrinsic carrier concentration, J_0 the saturation current density and V_{bias} is the external applied voltage with $V_b = \frac{V_{bias}}{V_C}$, $\nu_A = \frac{n_i}{N_A}$, $j_0 = J_0 \frac{L_n}{q D_p N_A} \frac{V_T}{V_C}$ and $s_n = S \frac{L_n}{D_n}$.

Remark 2.1 *The corresponding mathematical model for an n-type solar cell is completely analogous to (1)-(4), where the variable η is replaced by $\tau = \frac{p}{N_D}$ with p denoting the hole concentration.*

2.1 Solar cell simulator: KASCS

System (1)-(4) is solved numerically using the finite element method. An implicit - explicit variant of Newton's method is used to linearize the system and solve each equation separately thus reducing the computational cost considerably. Mesh adaptivity, see Figure 1(bottom), is used to resolve the Dirac-like behaviour of the incident light on the cell surface as well as to capture the steep gradients of the solution around the back contact. The solver was tested and compared with various well known open source solar cell simulators. Further details can be found in [23].

Various features are included in the solar cell simulator concerning shading, reflection and temperature effects. In particular,

- the cell surface texturing is assumed to be of pyramidical shape with angle of 45°;
- the effect on the incident solar irradiance of the geographical location and the tilt angle of the PV module, were also considered
- the shading of metallic grid and busbar was included
- the reflection of the incident light from the solar cell surface and the glass of the module was taken into account
- the dependance on temperature of various parameters of the problem: n_i, μ_n, μ_p, J_0 was also considered.

All the numerical results reported were obtained using linear finite elements. The computational domain was covered by a triangulation, which initially was adapted according to the variation of $g_n(z)$ and subsequently according to the solution iterates, see Figure 1(bottom). Part of the code was developed using the *FreeFem++* finite element computational framework [25]. The iterative scheme with mesh adaptivity converges in few iterations $1 \leq \ell_m \leq 4$ with a tolerance of 10^{-12} between two successive iterates. Further, the computational time to obtain an IV-curve consisting on the average of 120 points varied from $10 - 30$ min. We remark that our solver KASCS uses and adaptive algorithm to choose the voltage step in the calculation of an IV-curve. The numerous simulations were performed on the CRAY XC40(Shaheen) of the Supercomputing Laboratory at King Abdullah University of Science & Technology (KAUST) in Thuwal, Saudi Arabia.

3 Experimental setup

The outdoor experimental system is installed at KAUST in Thuwal, western region of Saudi Arabia at the New Energy Oasis (NEO) test field near the Red Sea coast (22.30 N, 39.10 E). The system consists of the following components:

- Two commercial PV modules, a monofacial and a bifacial one, with ground mounting system
- IV measuring system with radiation sensors
- Solar resource measurement station

The system components are analyzed in the following subsections.

3.1 PV modules and mounting systems

The modules selected for this study consist of a monofacial polycrystalline Si PV module and a bifacial monocrystalline Si, which are chosen to have similar electrical characteristics based on their manufacturer datasheets as shown on Table 1. The modules were installed in a standard Al profile mounting system with south facing orientation, where the system was designed to support various tilt angles. Testing was performed at $25, 45$ degrees tilt angles, with 20 cm module elevation. The ground is paved with grey coloured gravel. A picture of the installed modules at 25 degrees tilt is illustrated on Figure 2, where on the left is the location of the monofacial polycrystalline module, while on the right is the bifacial one. The modules were connected to an IV measuring system with multiple inputs in order to monitor the electrical characteristics of each one separately, as described in the next section.

3.2 Measuring system

The electrical output of each module was measured individually through an IV tracer system with multiple inputs. The system was designed and supplied by IMT Solar [26], using a high resolution IV curve analyzer, with a capacitive load and high speed data acquisition system capable of measuring a wide range of PV modules. The system is combined with a multiplexer to allow simultaneous measurements of multiple connected modules using 4 wire connections for IV measurements. Finally the setup includes an

Table 1: PV module specifications based on manufacturer's datasheets

PV module characteristics	Module 1(Monofacial)	Module 2(Bifacial)
Technology	Polycrystalline	Monocrystalline
Dimensions (cm)	166.5×99.1	165.6×98.4
Module type	Glass/backsheet, framed	Double Glass, frameless
Number of cells	60	60
Estimated Cell area (cm^2)	243.36	241.36
Maximum Power (W)	240	245
Maximum Current (A)	8.17	8.14
Maximum Voltage (V)	29.7	30.1
Short Circuit Current (A)	8.75	8.76
Open Circuit Voltage (V)	36.8	38.5
Fill Factor (%)	75.36	72.65
Module Efficiency (%)	14.5	15.1
NOCT (^oC)	45.7	48.9

Figure 2: Installed PV modules at 25 degrees tilt. On the left is the location of the monofacial polycrystalline module, while on the right is the bifacial one.

integrated industrial PC with Labview based data acquisition software to store the measured curves and sensor inputs (temperature and radiation). The whole system is integrated in a ventilated cabinet with a stainless steel hood to protect it from direct sunlight. Solar intensity is measured using two calibrated Si based irradiation sensors, connected at the front and back side of the module at the same inclination angle. The system is illustrated on Figure 3, while its specifications are listed on Table 2.

Figure 3: IV tracer system with multiple inputs for measuring the output of the monofacial and bifacial modules.

Table 2: IV tracer system technical specifications

IV tracer system technical data	
Data acquisition system	16 bit
Voltage Range (V)	$50 - 200$
Current Range (A)	$4 - 32$
Irradiance Range (W/m^2)	1300
Temperature Range (C)	$0 - 100$
Measuring time for IV curve (ms)	$2 - 500$
Maximum points per IV curve	4000
Number of PV module inputs	6

3.3 Solar resource measurement station

The solar resource measurement station is installed in the same outdoor field, near the site where the PV module measurement setup is located. The setup as shown on Figure 4 includes four sensors to perform precise measurements of the three solar radiation components: Spectral Global Horizontal Irradiance (s-GHI), Global Horizontal Irradiance (GHI), Direct Normal Irradiance (DNI), Diffuse Horizontal Irradiance (DHI) and the global spectral distribution (s-GHI). It also includes a sky camera to take hemispheric pictures of the sky. The system is designed and installed by TUV Rheinland who has installed a similar system for measuring solar and weather resources in KAUST as a part of the national research project PVKLIMA [27], while its sensors and cameras are supplied by EKO Instruments [28]. The system includes a standard sun-position sensor and GPS receiver. To measure the diffuse component of the solar radiation, a shading disk assembly is mounted on one arm of the tracker. The main specifications of the sensors are summarized on Table 3. The data acquisition system consists of a data-logger (Campbell
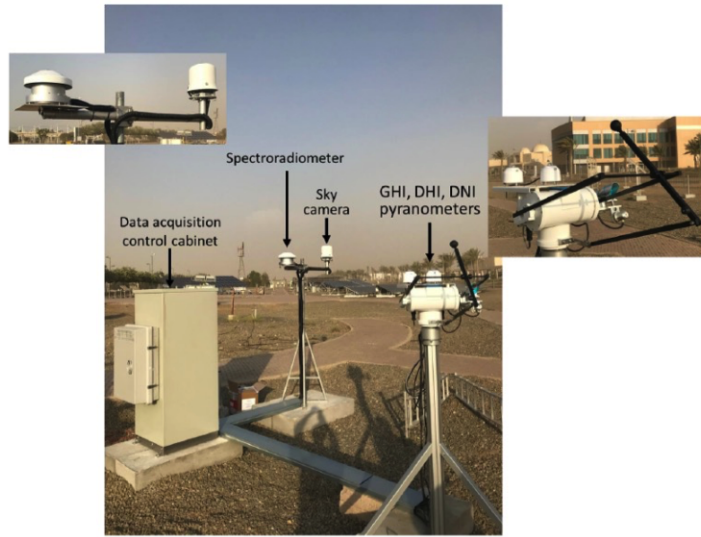
Figure 4: Solar resource monitoring station installed at KAUST NEO PV test site.

Table 3: Sensor specifications of the solar resource station

Specifications	Spectroradiometer	Pyranometers	Pyrheliometer	Sky camera
Measurement type	spectrum-GHI	GHI/DHI DNI	Hemispherical sky pictures	
Model	EKO MS-711	EKO MS-80	EKO MS-56	EKO ASI-16
Wavelength Range (nm)	$300 - 1100$	$285 - 3000$ nm	$200 - 4000$	N/A
Operating temperature range (^{o}C)	-10 to 50	-40 to 80	-40 to 80	-35 to 55
Other features	FOV 1800, Integrated temp. control (25 ^{o}C)	ISO 960 Secondary Standard	ISO 960 First Class	5 MP resolution, FOV 1800, Integrated temp. control

Scientific CR1000 [29]) to record sensor data over time. The solar data and sky images are also collected at specified time intervals. The electronic components are housed in a cooled cabinet to maximize their

lifetime in hot-humid outdoor conditions. The system is equipped with a UPS to keep the measurement running for 2 hours in case of a power shortage.

3.4 Data acquisition - Measurements

The experiments on both PV modules were conducted in two different time periods each corresponding to a different tilt angle as it's shown in Table 4. During these periods we have recorded on a daily

Table 4: Time periods and PV module tilt angles.

Time Period	Tilt angle
28/03/2018 - 06/04/2018	25
23/04/2018 - 05/05/2018	45

basis and at 5 minutes interval the direct and reflected solar irradiance, solar spectrum and ambient temperature. The IV curves of both PV modules were also measured with the same frequency providing us with operational characteristic quantities of the modules such as V_{oc} and I_{sc}. The material used for PV module encapsulation is considered as EVA-type, where its reflection coefficient was measured using an encapsulated glass - EVA sample with an Agilent Cary 7000 universal measurement spectrophotometer, using the integrating sphere technique, is shown in Figure 5. All these measurements are used to setup
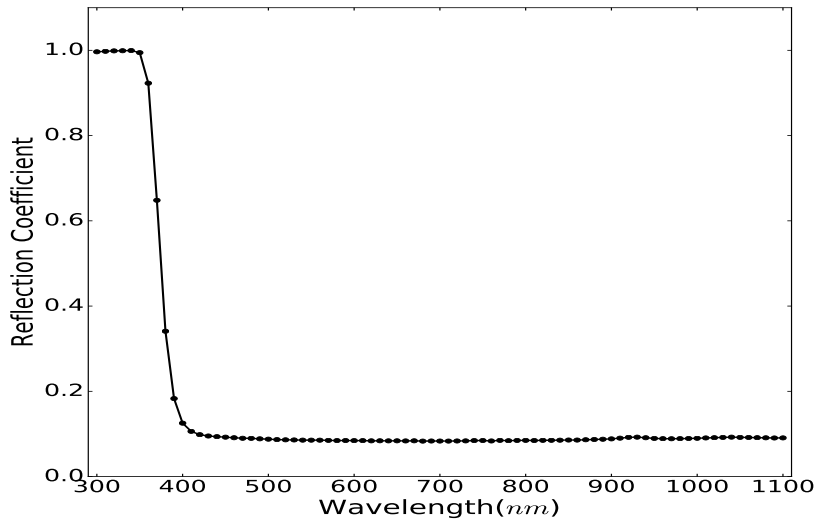
Figure 5: Reflection coefficient of EVA-type glass

our solar cell simulator.

4 Simulations - Experimental results

4.1 Simulation characteristics and parameters

The simulated bifacial PERC type solar cell structure is illustrated in Figure 1(left), where the emitter is covering the front surface, while the back surface is passivated and the contacts are stripe-shaped due the considered 2D geometry. The cell base substrate is n-type with uniform doping density $N_D = 10^{16} cm^{-3}$, while carrier mobility values and intrinsic concentration are taken from [30]. We also assume an ideal thin emitter covering the entire front surface, where photogeneration is occurring in the base only, while the base emitter saturation current is $J_0 = 10^{-13} A/cm^2$. The recombination velocity at the back passivated area is considered $S_1 = 10 \ cm/s$, which is typical of silicon oxide or nitride passivation layers [31], while at

the back contacts is calculated by the following expression: $S_2 = \dfrac{J_{0C}N_D}{q\,n_i^2}$, where J_{0C} is the recombination current at the back contact which is assumed as $J_{0C} = 4 \cdot 10^{-12} A/cm^2$. This surface recombination value corresponds to a recombination velocity within the range observed for Al-BSF laser fired contacts used in PERC solar cells [32]. The simulated monofacial PERC solar cell is p-type Al-BSF structure with uniform base doping density $N_A = 10^{16} cm^{-3}$, where carrier mobilities and intrinsic concentration taken from [30]. The base emitter saturation current and velocity S_2 are taken as in the bifacial cell, while $J_{0C} = 10^{-12} A/cm^2$. In both solar cells the metallic grid fingers have width $100\mu m$ which is assumed to be in the centre of the cell, while the busbar reduces the incident light by 2.3%. In the simulations we assume that each cell has length $p = 1200\mu m$ and width $w = 180\mu m$, see Figure 1(left, right). The back contact covers the whole back surface of the cell in the mofacial module while in the bifacial one it is at 10% of its length.

The effect of the location and tilt angle of module on the incident solar irradiance is also accounted for. For the aforementioned time periods the corresponding coefficient C_S, which scales the solar irradiance, was found to vary considerably mainly due to the tilt angle: $C_S \in [1.05915, 0.994513]$ for 25° tilt angle, $C_S \in [0.832718, 0.783781]$ for 45° tilt angle.

The solar cells themselves also reflect light and this is also considered in our simulations. The corresponding reflection coefficients for the monofacial and bifacial solar cells were obtained from [30].

4.2 Temperature effects

One of the most important factors affecting solar cell operation is temperature. In the literature, most studies assume that the cell operates under nominal (STC) conditions(25^oC) which is not the case in reality. In many areas of the Middle East region the ambient temperature can rise several degrees above nominal conditions and module temperature can reach as high as 60^oC or more. Temperature affects several material parameters, which can considerably reduce PV module efficiency. These temperature effects are incorporated in our solar cell simulator.

In the literature there are several models for estimating the PV module operating temperature. A set of models use electrical characteristics of the module, e.g. V_{oc} and/or I_{sc} which under operating conditions they are not available. Another group of models use parameters which, in general, are available a priori, such as air temperature(T_{air}), solar irradiance(G_{irr}), wind velocity(v_w) and efficiency of the module(η_{ref}). In this study we focus on such type of models, see [33], [34], [35], [36], [37] respectively, where all the involved quantities are provided a priori either by the manufacturer, see Table 1, or by our measurements:

$$T_c^t = T_{air} + \frac{G_{irr}}{800}(T_{NOCT} - 20)(1 - \eta_m)\left(\frac{9.5}{5.7 + 3.8v_w}\right), \quad (^oC) \tag{5}$$

$$T_c^S = T_{air} + 0.0138G_{irr}(1 + 0.031T_{air})(1 - 0.042v_w)(1 - 1.053\eta_m), \quad (^oC) \tag{6}$$

$$T_c^C = 0.943T_{air} + 0.028G_{irr} - 1.528v_w + 4.3, \quad (^oC) \tag{7}$$

$$T_c^L = 30.006 + 0.0175(G_{irr} - 300) + 1.14(T_{air} - 25), \quad (^oC) \tag{8}$$

$$T_c^K = T_{air} + G_{irr}e^{-3.473 - 0.0594v_w}, \quad (^oC). \tag{9}$$

To assess the effectivity of (5)-(9) we setup an experiment where the temperature of both modules was measured for a period of six days in July 2018 during sunlight hours and sampled every five minutes. The wind values were obtained from a TMY of [38] for the location of KAUST university. The behaviour of the five models is shown in Figure 6 along with the measurements T^m(red line). It should be noted that the measured module temperature do not represent actual PV cell operating temperature because the sensors are attached to the insulated (backsheet or glass) back module surface. This measurement deviation also depends on the type of the sensor used, its attachment method, as well as weather conditions such as irradiance and wind speed [39]. The root mean square differences(RMSD) for each model is also depicted in the figure. All models agree very well with measurements during morning and afternoon hours of the day, while substantial differences are observed around noon hours, where temperature reach peak values. The curve representing the measurements lie in between the predictions of the models, however, it is apparent that there is no clear advantage of using any particular model among (5)-(9). Based on this observation we proceed by taking a linear combination of all aforementioned models to estimate the
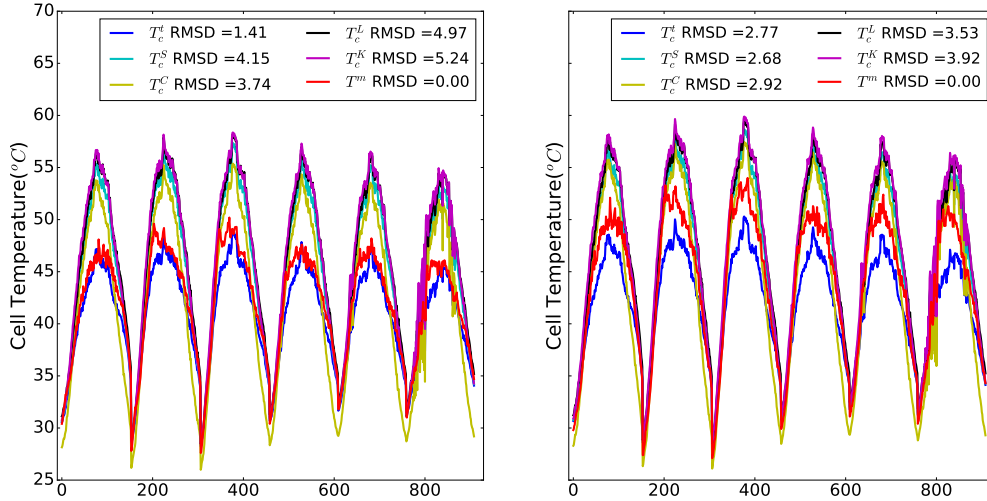
Figure 6: PV module temperature models performance: Monofacial(left), Bifacial(right).

module temperature :

$$T_c^{LS} = w_t\ T_C^t + w_S\ T_c^S + w_C\ T_c^C + w_L\ T_c^L + w_K\ T_c^K, \tag{10}$$

where w_t, w_S, w_C, w_L, w_K are real numbers to be determined by linear least square fitting to the measurements. At this point we can use the whole or part of the dataset of measurements to *train* the weights. In Table 5 the corresponding RMSD's are shown using from one up to six days of measurements. It was observed that essentially the RMSD value remains unchanged using only half of the dataset with less than of 1^oC of difference. The weights obtained using the whole set of measurements are shown in

Table 5: Training days and corresponding RMSD's

Days	1	2	3	4	5	6
Monofacial	1.145	0.804	0.762	0.748	0.739	0.738
Bifacial	1.309	1.023	0.985	0.958	0.942	0.936

Table 6. These values depend on the underlying module technology but they are independent of the tilt angle and will be used in the sequel to estimate the PV modules operating temperatures for both periods of testing. The effectiveness of this approach is demonstrated further in Figure 7 where the measured values of module temperature and their estimation by T_c^{LS} are shown. According to the estimation

Table 6: Weights of T_c^{LS} obtained from the whole dataset

Weights	w_t	w_S	w_C	w_L	w_K
Monofacial	0.68063	2.05398	-0.77271	-2.01659	1.01839
Bifacial	-0.00491	2.06415	-1.10514	-2.22521	2.15693

of PV module operating temperature provided by T_c^{LS} we modify several material parameters affected by the temperature. The main focus was on parameters with significant contribution to PV module operation: a) silicon light absorption coefficient($\alpha(\lambda)$), b) intrinsic carrier concentration(n_i), c) carrier mobilities μ_n, μ_p, d) saturation current density J_0, J_{0C}, e) electron lifetime τ_n.

The temperature effects on the light absorption coefficient are calculated using an exponential law proposed in the study by M.A. Green [40]. To account for the changes on intrinsic carrier concentration and carrier mobilities, the study of PVLiighthouse [30] was considered. In particular for temperatures
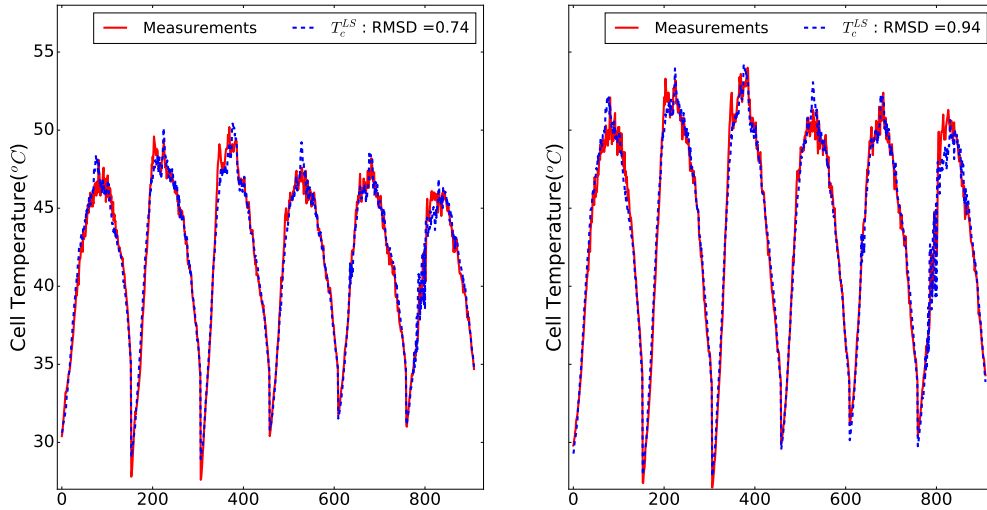
Figure 7: Least squares approximation T_c^{LS} : Monofacial(left), Bifacial(right).

ranging from $280^o K$ to $370^o K$ with step of $10^o K$ we obtain the corresponding values of carrier intrinsic concentration and mobilities. For any value of the temperature T_c^{LS} in this range the required value is computed by linear interpolation. The other two quantities, J_0, τ_n, are a little bit more involved. For saturation current we follow the approach suggested in [41] which expresses J_0 in terms of energy bandgap and a nonlinear temperature term. Concerning the electron lifetime τ_n the model proposed in [42] was used.

Remark 4.1 *This is the first exploratory step to study the effect of temperature in solar cell operation focused only on the variation of certain material parameters affected by thermal changes and their effect in the cell performance. A more comprehensive approach to evaluate the temperature effects in solar cells would have to include also an energy equation in the mathematical model. This goes beyond the current scope and will be the subject of future work.*

4.3 Resistance effects

The mathematical model and the solar simulator don't include any external resistance effects related to PV module and system design, which are influenced by cell interconnection in series or parallel, cabling losses as well as current mismatches between different cells. Commonly in PV modules *series* and *shunt* resistances due to these factors are important sources of power output loss. Our goal is to estimate these resistances and account for their effect by correcting-modifying the simulated IV-curves on a posteriori way. In the literature several ways were proposed to estimate these resistances see e.g. [43] and the references therein. In this work, a different approach based on the experimental data collected was followed. The effect of both series and shunt resistances is given by the well known formula

$$ I = I_{sc} - I_0 \left(\exp\left(\frac{V + I\,R_s}{m\,V_T} \right) - 1 \right) - \frac{V + I\,R_s}{R_{sh}} \ , \tag{11} $$

where $V_T = \frac{\kappa T}{q}$ is thermal voltage, while the saturation current I_0, resistances R_s, R_{sh} and ideality factor m are unknown quantities to be determined. To estimate these parameters we use the available measurements and nonlinear least squares approximation. We proceed then to correct the simulated IV-curve and compute its characteristic quantities by solving the equation (11). The procedure we follow is now described in detail.

The estimation of the parameters will be done in a gradual way, thus at every step of the process one parameter will be determined and take a definite value. First we take, without loss of generality,

10

$m = 1$. The value of I_0 is computed by the data of the simulated IV-curve using the following well known formula, while the temperature is estimated following the process described in the previous section,

$$V_{oc} = mV_T \log \left(\frac{I_{sc}}{I_0} + 1 \right) \implies I_0 = I_{sc} \left(e^{\frac{V_{oc}}{mV_T}} - 1 \right)^{-1} . \tag{12}$$

To estimate the resistances R_s, R_{sh}, we perform first a nonlinear least square fitting to (11) for all experimental IV-curves with irradiance greater than $800W/m^2$. It was observed that the series resistance, with an average value $R_s^{avg} = 2.02$ and standard deviation $R_s^{std} = 0.026$, remained the same for both monofacial and bifacial modules, tilt angles and its dependence on temperature and solar irradiance is negligible. A typical example of this behaviour of R_s is shown in Figure 8. Motivated by the distribution
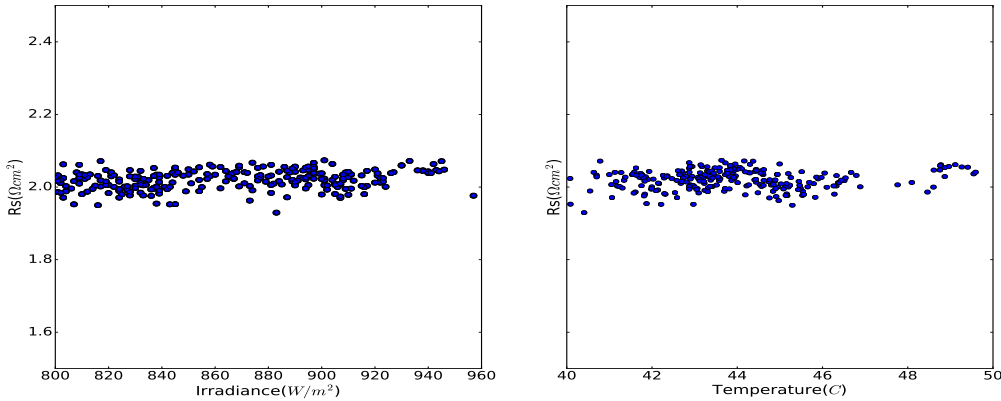
Figure 8: Distribution of series resistance R_s

of the values of R_s we set $R_s = 2$ in (11) and we perform another nonlinear least square fitting to estimate the shunt resistance R_{sh}. There is no clear dependence of R_{sh} from the temperature, however R_{sh} decreases linearly with respect to solar irradiance, [44]. Table 7 shows the coefficients of the corresponding linear least square fitting for each module and tilt angle. To recap, for a given simulated IV-curve its

Table 7: Least square fitting of R_{sh} with respect to solar irradiance G_{irr}

Monofacial, 25°	$R_{sh} = -0.759 \, G_{irr} + 1089$
Monofacial, 45°	$R_{sh} = -0.705 \, G_{irr} + 966$
Bifacial, 25°	$R_{sh} = -0.397 \, G_{irr} + 663$
Bifacial, 45°	$R_{sh} = -0.494 \, G_{irr} + 787$

correction is obtained by taking $m = 1$, $R_s = 2$, I_0 from (12), R_{sh} from Table 7 and solving (11).

4.4 Daily yield output

In this section we first compare various characteristic quantities of the PV modules obtained from the simulations with the corresponding ones from measurements. The time series over both time periods of maximum power P_{wr}, V_{oc}, I_{sc} are shown in the following Figures 9, 10 for monofacial and bifacial device for the two tilt angles. The high oscillatory behaviour observed in power and current for both devices during the first period, Figures 9, 10 is not related to the tilt angle but it's due to the presence of a light sandstorm in the area. This type of phenomena are quite typical in the middle eastern countries resulting in substantial reduction of the direct solar irradiance, see also Figures 14, 15. During the second period with tilt angle 45°, no such phenomenon occurred, which is evident by the oscillations-free smooth daily variations of the relative quantities and also reflected on the corresponding RMSD values, see Table 8. It's also worth noticing the very close match of short circuit current between simulations

Table 8: RMSD values of module characteristic parameters

	Period 1 (tilt angle 25°)		Period 2 (tilt angle 45°)	
	MF	BF	MF	BF
P_{wr}	24.0822	25.9262	11.9460	13.4741
V_{mp}	0.0521	0.0617	0.0505	0.0570
I_{mp}	0.0032	0.0028	0.0014	0.0015
V_{oc}	0.0147	0.0058	0.0141	0.0064
I_{sc}	0.0030	0.0028	0.0017	0.0019
FF	0.0960	0.1180	0.0983	0.1115

and experimental values for both devices and tilt angles, which is a result of using exact spectral data to perform the simulations. In Figures 11, 12 the daily yield output (kwh/kwp) is shown for each tilt angle. In each figure the left graph is for the monofacial module while the right graph refers to the bifacial one. Both graphs show good agreement with the experimental curves following exactly the measured daily energy yield changes, thus validating our model. A third curve is also shown in each graph corresponding to the *corrected*-simulated IV-curve taking into account PV module series and shunt resistance following the correction process described in the previous section. The agreement of corrected daily yield output with the experimental data is remarkable thus validating the aforementioned correcting process. Table 9 shows the absolute and relative differences, measured in the discrete 2-norm of simulated and corrected daily yield output with respect to experimental data for the whole time period.

Table 9: Absolute and relative differences of simulated and corrected simulated daily yield output with respect to measurements

	Simulated		Corrected	
	Abs-Diff(kwh/kwp)	Rel-Diff(%)	Abs-Diff(kwh/kwp)	Rel-Diff(%)
Monofacial, 25°	2.67	26.05	1.022	9.96
Monofacial, 45°	1.74	14.86	0.076	0.65
Bifacial, 25°	2.78	24.43	0.733	6.43
Bifacial, 45°	2.03	15.42	0.101	0.76

Figure 13 shows the simulated and experimental relative energy gain of the bifacial module compared to the monofacial one for the 25 and 45 degree angles respectively. Both graphs show that the experimental and simulated curves are very close with each other, thus verifying the accuracy of the bifacial model simulation. The bifacial module installed at 45 degrees show slightly higher energy gain compared to the 25 degrees installation as expected due to increased irradiance on the back surface as a result of the higher tilt angle. It is worth noting, that in the case of the 25 degrees installation, for a specific period (March 28th till April 4th), the simulated bifacial power gain underestimates the corresponding experimental one quite significantly. This is related to the sandstorm mentioned earlier and can be attributed to the increased diffused component of the solar radiation where light is scattered by the airborne dust particles as already mentioned in our previous work [23]. To further investigate the effects of the dust storm, a comparative plot of the global sunlight spectra at noon ($12:30\ pm$) for two different dates is illustrated on Figure 15. The AM1.5 Global is also added as a reference. The spectrum on March 28th (black curve) is received on a clear day before the sandstorm, while the one on April 4th (blue curve) is after the event, where the relatively high concentration of airborne dust particles has changed the color of the sky from blue to a yellowish tint as also shown on the sky camera snapshot of Figure 14. The comparison of both spectra show that after the sandstorm event, the intensity of the solar spectrum has been significantly reduced, especially at UV and visible wavelengths, while at near IR region (beyond $800nm$) it remains almost unchanged. This spectrum change also affects PV module performance as already mentioned.
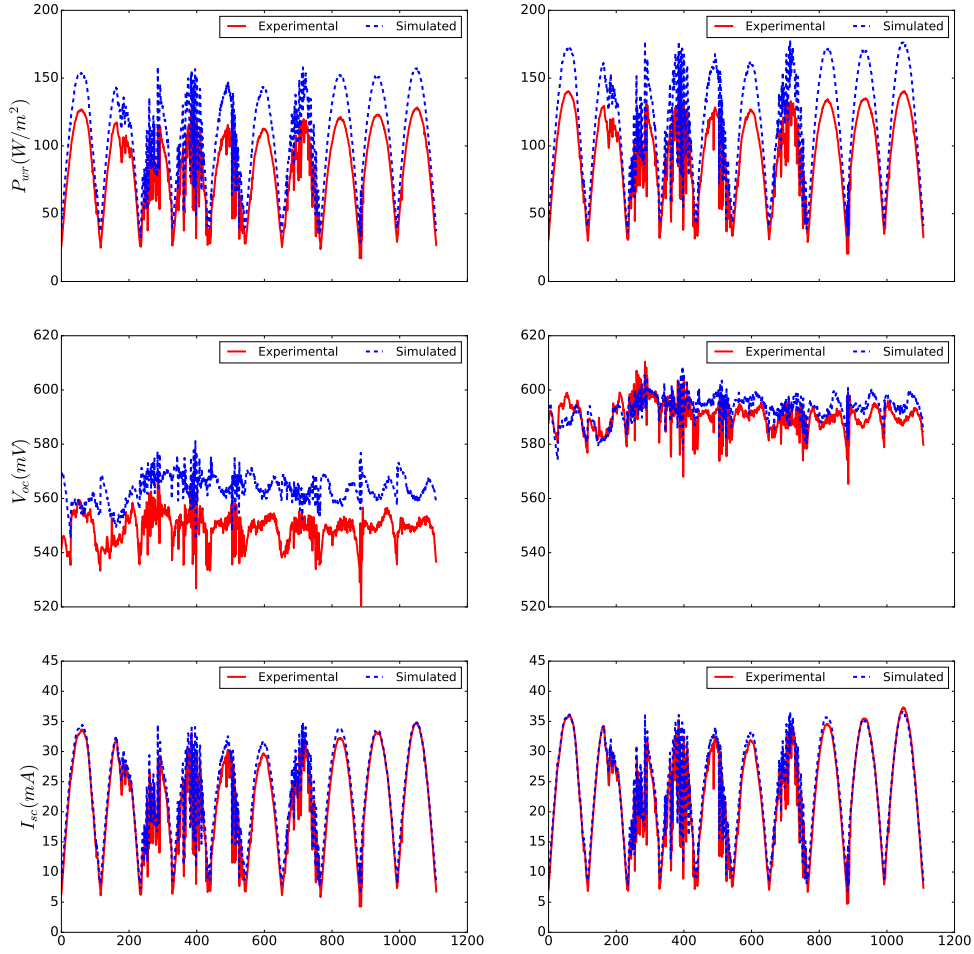
Figure 9: Comparison of measured(red solid line) and simulated(blue dashed line) results at 25° : Monofacial(left), Bifacial(right)

5 Discussion

The previous section describes the application of our developed model, which is customized to simulate bifacial structures, and validated with experimental data. The custom model is based on the solution of the 2D solar cell device transport equations. The solver is based on the finite element method and uses mesh adaptivity to capture the Dirac like behaviour of the incoming light on the top surface and the steep gradients of the solution around the back contact of the complicated PV structure. Further, it implements an adaptive algorithm to choose the voltage step in the calculation of an IV-curve. A novel approach was presented to calculate the module temperature by taking a linear combination of various temperature models though linear square fitting. The customized model also incorporates locally measured solar spectra for precise calculation of actual PV module performance. This is an important aspect, since it has been already demonstrated in [45] that both shape and power of solar spectrum have an important weight on PV module performance. The results demonstrate that the bifacial structure has a significant energy yield advantage compared to the monofacial one. There is a 10% energy gain of the bifacial module over the monofacial one for the 25° angle while the corresponding gain for the 45° tilt angle is about 15%. Although our assessment was based on a specific experimental setup, other aspects could be investigated such as the ground albedo using materials with higher reflectivity, and increased

13
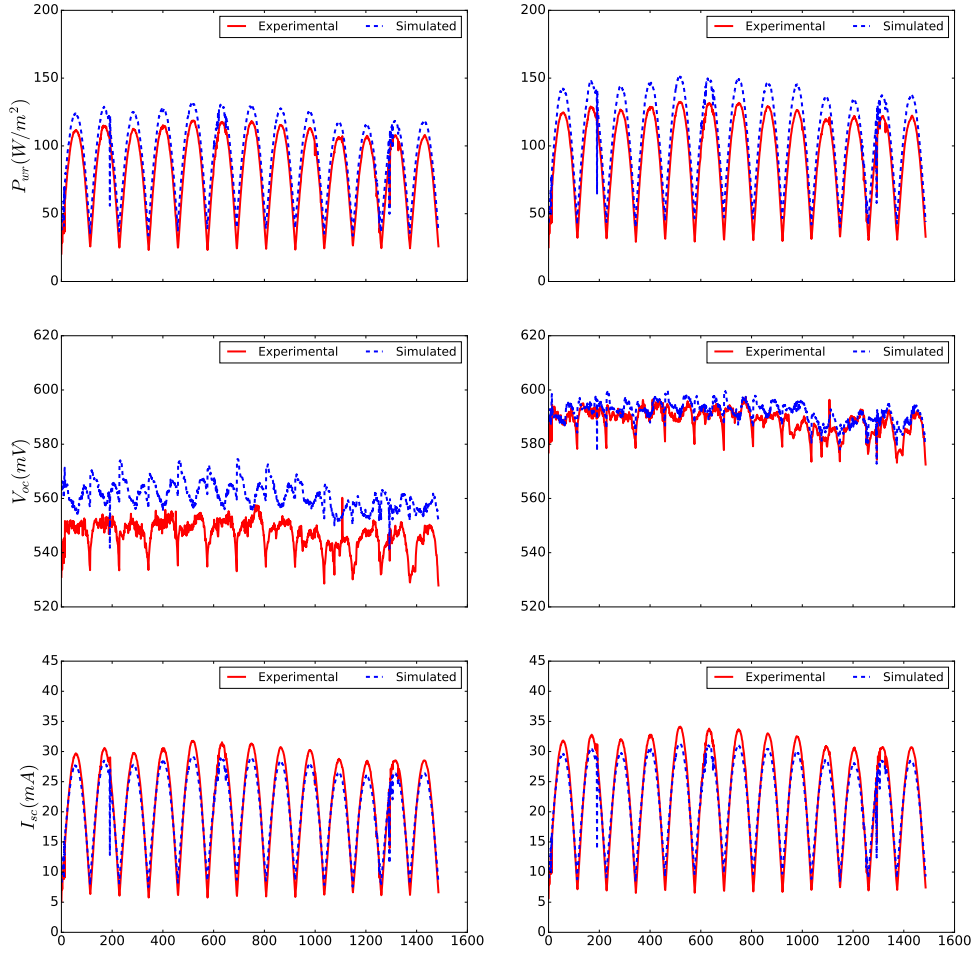
Figure 10: Comparison of measured(red solid line) and simulated(blue dashed line) results at 45° : Monofacial(left), Bifacial(right)

bifacial module elevation to increase incoming light from the back surface. Furthermore, ground material may not have uniform reflectivity for all light wavelengths absorbed by the module which, in turn, can have significant impact on the bifacial module performance [46]. Such effects were not currently taken into account into our simulations, however they can be easily added into the model by using detailed reflectance curves of the ground material.

In addition, using proper statistical analysis and advanced prediction algorithms on long term weather data like temperature and solar spectrum, this customized model may predict with high accuracy bifacial and monofacial module energy yield. This is important for the Middle East region, where dust storms significantly affect solar radiation by scattering light and alter sunlight spectrum. Such effects can provide a specific advantage for the bifacial devices due to increased diffuse light entering the back surface and should be investigated in detail.

6   Conclusions

We have presented a series of comparisons between experimental data obtained from a set of one monofacial and a bifacial PV module installed nearby the western coast of Saudi Arabia and the results of a
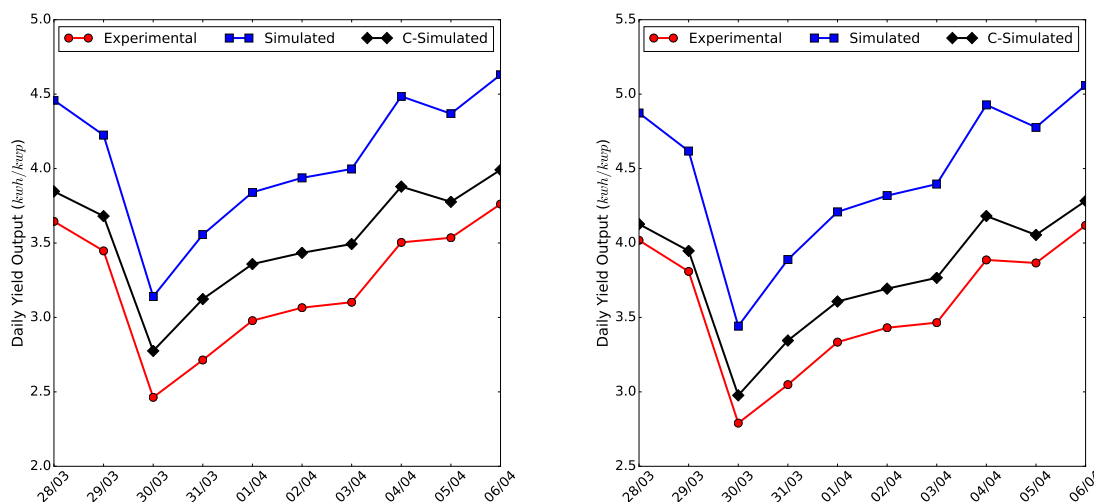
Figure 11: Daily yield output(kwh/kwp) for 25° tilt angle: Monofacial(left), Bifacial(right)

customized solar cell device simulator developed to take into account spectral and temperature effects. The simulated results predict very well the daily yield output for both devices. The bifacial device shows a gain of 10% and 15% for 25° and 45° tilt angle, respectively, when compared to the monofacial one. Our results further suggest that for PV installations in the Middle East region where sandstorms are frequent, it would be beneficial using bifacial devices over monofacial ones since they can absorb more of the diffused sunlight which is in abundance when such phenomena occur.

Acknowledgments

References

[1] S. Wanga, O. Wilkieb, J. Lam, R. Steeman, W. Zhang, K-S Khoo, S-C Siong, and H. Rostan. Bifacial photovoltaic systems energy yield modelling. *Energy Procedia*, 77:428 – 433, 2015.

[2] Y. Chieng and M.A. Green. Computer Simulation of Enhanced Output from Bifacial Photovoltaic Modules. *Progress in Photovoltaics: Research & Applications*, 1:293–299, 1993.

[3] T. Joge, Y. Eguchi, Y. Imazu, I. Araki, T. Uematsu, and K. Matsukuma. Applications and field tests of bifacial solar modules. In *Proc. 29th IEEE PV Specialists Conference*, pages 1549–1552, 2002.

[4] J. Libal, D. Berrian, and R. Kopecek. Energy yield simulations and calculation of lcoe for bifacial pv system. In *bifi PV Workshop, Konstanz, Germany*, 2017.

[5] https://www.pv-tech.org/news/acwa-power-wins-saudi-300mw-solar-project 2018.

[6] T. Warabisako, K. Matsukuma, S. Kokunai, Y. Kida, T. Uematsu, and H. Yagi. Bifacial multicrystalline Silicon solar cells. In *Proc. 23rd IEEE PV Specialists Conference*, pages 248–251, 1993.
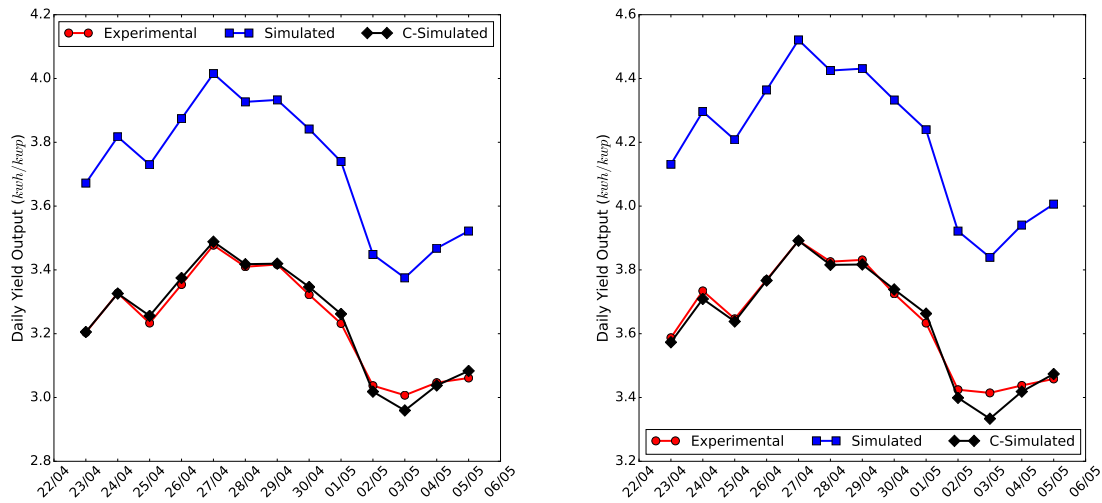
Figure 12: Daily yield output(kwh/kwp) for 45° tilt angle: Monofacial(left), Bifacial(right)

[7] A. Moehlecke, I. Zanesco, and A. Luque. Practical high efficiency bifacial solar cells. In *Proc. 24th IEEE PV Specialists Conference*, pages 1663–1666, 1994.

[8] SolarWorld. SunModule, BiSun, http://www.solarworld.de.

[9] Trinasolar. DUOMAXtwin, http://www.trinasolar.com.

[10] Sunpreme. GxB series, http://sunpreme.com/gxb-series-2.

[11] NEO Solar Power Corporation (NSP). BiFi Series, http://www.nsp.com/s/2/product-c73729/BiFi-Bifacial-Cell.html.

[12] ITRPV. International Technology Roadmap for Photovoltaic Results 2016. Technical report, ITRPV, 2017.

[13] A. W. Blakers, A. Wang, A. M. Milne, J. Zhao, and M. A. Green. 22.8 % efficient silicon solar cell. *Applied Physics Letters*, 55(13):1363, 1989.

[14] I. Romijn, I. Cesar, M. Koppes, E. Kossen, and A. Weeber. Pasha: A new industrial process technology enabling high efficiencies on thin and large mc-Si wafers. In *IEEE Photovoltaic Specialists Conference*, 2008.

[15] Yingli Solar. Bifacial modules, http://www.yinglisolar.com/en/products/solar-modules/.

[16] M. Taguchi, A. Yano, S. Tohoda, K. Matsuyama, Y. Nakamura, T. Nishiwaki, K. Fujita, and E. Maruyama. 24.7 % Record Efficiency HIT Solar Cell on Thin Silicon Wafer. *IEEE Journal of Photovoltaics*, 4(1):96–99, 2014.

[17] M. Burger. Heterojunction technologies, https://www.meyerburger.com/gr/en/technologies/photovoltaics/high-efficiency-technologies/heterojunction/.

[18] X. Sun, M. R. Khan, C. Deline, and M.A. Alam. Optimization and performance of bifacial solar modules: A global perspective. *Applied Energy*, 212:1601–1610, 2018.

[19] PVSyst. Photovoltaic software, http://www.pvsyst.com/en/.

[20] Valentin Software. Photovoltaic software, https://www.valentin-software.com/en/products/.

[21] Laplace Systems. SolarPro, http://www.laplacesolar.com/photovoltaic-products/solar-pro-pv-simulation-design/.
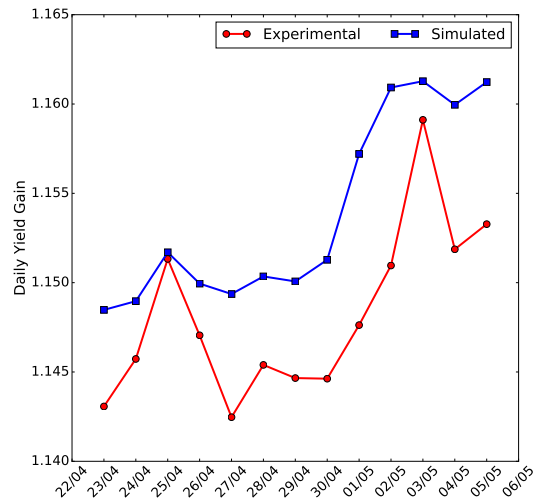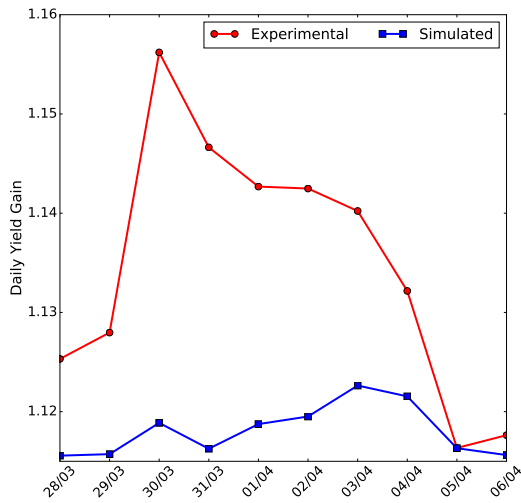
Figure 13: Daily energy yield gain : Bifacial / Monofacial for 25^o(left), 45^o(right)
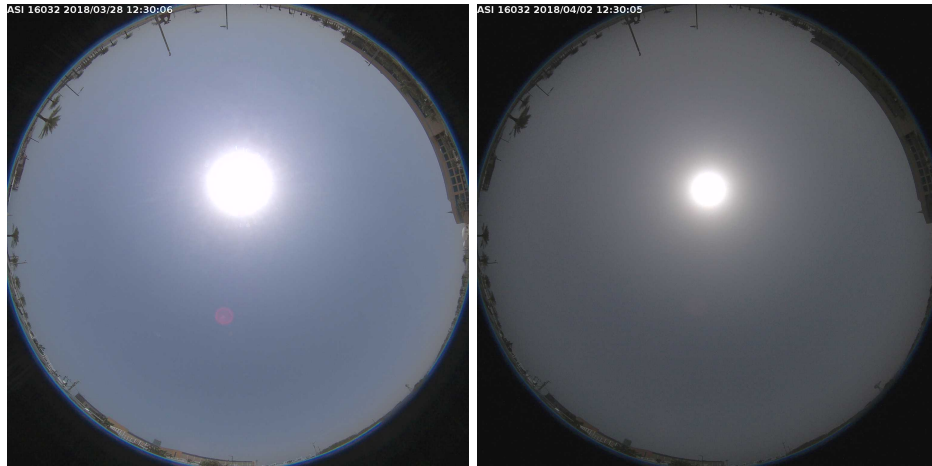
Figure 14: Sky camera snapshot at $12:30$ local time : 2018/03/28(left), 2018/04/02(right)

[22] Archeliospro. PV simulation software, http://www.archelios.com/pvsoftware.php.

[23] Th. Katsaounis, K. Kotsovos, I. Gereige, A. Al-Saggaf, and A. Tzavaras. 2d simulation and performance evaluation of bifacial rear local contact c-si solar cells under variable illumination conditions. *Solar Energy*, 158:34–41, 2017.

[24] K. Kotsovos and K. Misiakos. Three-dimensional simulation of carrier transport effects in the base of rear point contact silicon solar cells. *Journal of Applied Physics*, 89(4):2491–2496, 2001.

[25] F. Hecht. New development in FreeFem++. *J. Numer. Math*, 20:251–265, 2012.

[26] IMT solar. https://www.imt-solar.com/.

[27] PVPMC. Modeling collaborative workshop, IEA-PVPS T13-06, 2017.

[28] EKO Instruments. https://eko-eu.com/.

[29] Campbell Scientific. https://www.campbellsci.com/cr1000.

[30] PV-Lighthouse. https://www.pvlighthouse.com.au.
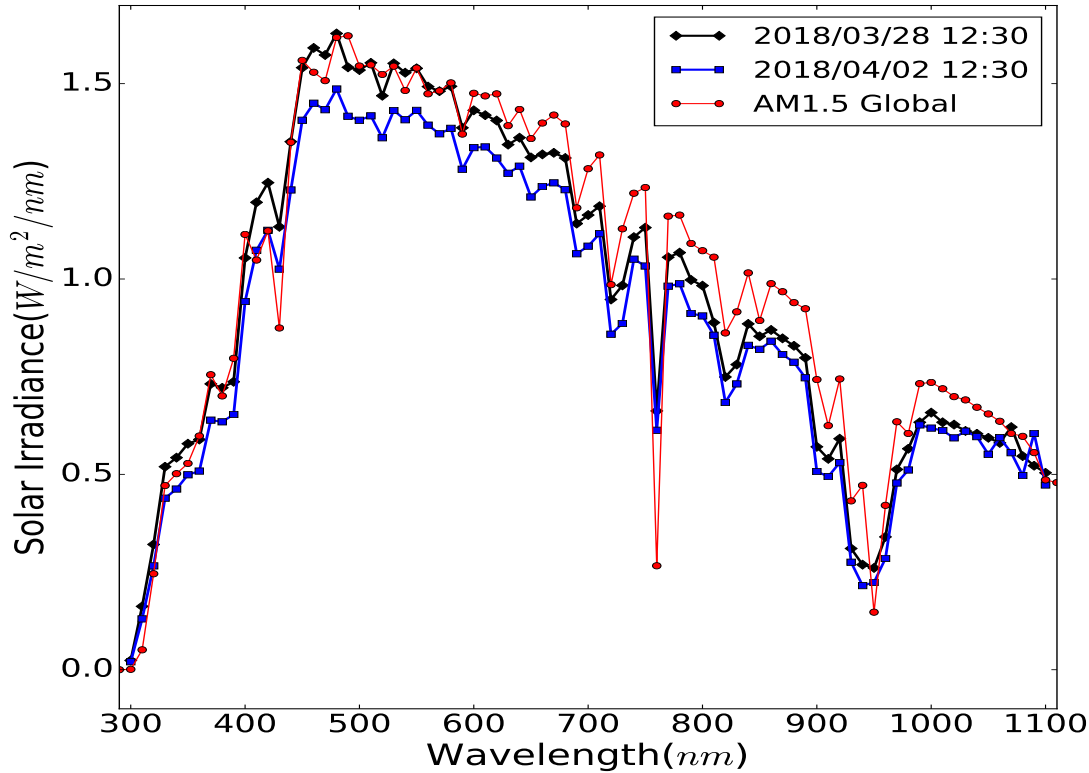
Figure 15: Spectrum comparison measured for 2 different dates at noon (12:30 pm local time) and the Global AM15 reference.

[31] M. Zanuccoli, R. DeRose, P. Magnone, E. Sangiorgi, and C. Fiegna. Performance Analysis of Rear Point Contact Solar Cells by Three-Dimensional Numerical Simulation. *IEEE Transactions on Electron Devices*, 59(5):1311–1319, 2012.

[32] R. Horbelt, G. Micard, P. Keller, R. Job, G. Hahn, and B. Terheiden. Surface recombination velocity of local Al-contacts of PERC solar cells determined from LBIC measurements and 2D simulation. *Energy Procedia*, 92:82–87, 2016.

[33] J. A. Duffie and W. A. Beckman. *Solar Engineering of Thermal Processes*. Wiley, 2006.

[34] J. M. Servant. Calculation of the cell temperature for photovoltaic modules from climatic data. In *Proceedings of the 9th biennial congress of ISES- Intersol 85*, 1985.

[35] R. Chenni, M. Makhlouf, T. Kerbache, and A. Bouzid. A detailed modeling method for photovoltaic cells. *Energy*, 32:1724–1730, 2007.

[36] F. Lasnier and T. G. Ang. *Photovoltaic engineering handbook*. Adam Hilger, 1990.

[37] D. L. King, W. E. Boyson, and J. A. Kratochvill. Photovoltaic array performance model, 2004.

[38] EU-IET. Photovoltaic geographical information system (http://re.jrc.ec.europa.eu/pvgis/).

[39] S. Krauter and A. Preiss. Comparison of module temperature measurement methods. In *34th IEEE Photovoltaic Specialists Conference (PVSC)*, 2009.

[40] M. A. Green. Self-consistent optical parameters of intrinsic silicon at 300 k including temperature coefficients. *Solar Energy Materials & Solar Cells*, 92:1305–1310, 2008.

[41] P. Singh and N.M. Ravindra. Temperature dependence of solar cell performance—an analysis. *Solar Energy Materials & Solar Cells*, 101:36–45, 2012.

[42] D.B.M. Klaassen. A unified mobility model for device simulation–ii. temperature dependence of carrier mobility and lifetime. *Solid State Electronics*, 35(7):961–967, 1992.

[43] K.C. Fong, K.R.McIntosh, and A.W. Blakers. Accurate series resistance measurement of solar cells. *Prog. Photovolt: Res. Appl.*, 21:490–499, 2013.

[44] M. Chegaar, A. Hamzaoui, A. Namoda, P. Petit, M. Aillerie, and A. Herguth. Effect of illumination intensity on solar cells parameters. *Energy Procedia*, 36:722–729, 2013.

[45] Aitor Marzo, Pablo Ferrada, Felipe Beiza, Pierre Besson, Joaquín Alonso-Montesinos, Jesús Ballestrín, Roberto Roman, Carlos Portillo, Rodrigo Escobar, and Edward Fuentealba. Standard or local solar spectrum? implications for solar technologies studies in the atacama desert. *Renewable Energy*, 127:871–882, 2018.

[46] T. Russell, R. Saive, A. Augusto, S. Bowden, and H. Atwater. The influence of spectral albedo on bifacial solar cells: A theoretical and experimental study. *IEEE Journal of Photovoltaics*, 7(6):1611–1618, 2017.